Open Ceramics 26 (2026) 100981

Contents lists available at ScienceDirect

Open Ceramics

journal homepage: www.sciencedirect.com/journal/open-ceramics

Rapid radiation sintering of additively manufactured large-sized alumina tetrahedrons

Aljaž Iveković [a,1], Miha Križaj [b,1], Andraž Kocjan [a,*]

[a] Department for Nanostructured Materials, Jožef Stefan Institute, Jamova 39, Sl-1000 Ljubljana, Slovenia
[b] Jožef Stefan International Postgraduate School, Jamova 39, 1000, Ljubljana, Slovenia

A R T I C L E I N F O

Keywords:
Additive manufacturing
Fused filament fabrication
Pressureless spark plasma sintering
Ultrafast high-temperature sintering
Alumina

A B S T R A C T

Rapid radiation techniques, such as pressureless spark plasma sintering (pSPS) and ultra-fast high-temperature sintering (UHS), have proven effective in achieving rapid densification of ceramics, including additively manufactured components. However, sintered component sizes tend to be small, disk-shaped or having thin-strutted geometries. Here, fused filament fabrication (FFF) of a commercial filament was used for manufacturing complex-shaped and large-sized alumina tetrahedra with edge thickness of 5 mm, varying the edge size (15–40 mm). The aim was to investigate the effect of heating rate (33–300°C/min) and tetrahedron size on the pSPS outcome. The pSPS reductive environment discoloured the tetrahedra, but were all successfully rapidly sintered to full density irrespective of their size and heating rate employed. The evolved thermal gradient contributed to differential, anisotropic densification related shrinkage, microstructure and mechanical properties specific to tetrahedra` edge position, i.e., core versus shell and base versus lateral, also triggering cracking of the largest tetrahedra.

1. Introduction

Additive manufacturing (AM) of ceramics has emerged as a key shaping technology for applications in automotive, aerospace, biomedical, and environmental fields—including catalysis and electrochemical systems—where complex geometries or multimaterial components with enhanced functionality and efficiency are required [1–3]. Among many available AM techniques lithography-based ceramic manufacturing (LCM) is established as the most advanced, allowing consolidation of fine ceramic powders dispersed in a photosensitive polymer [4] and, thus, facilitating components with intricate features with superior surface finish [5]. Despite its advantages, LCM is expensive and time-consuming process [3], requiring a lengthy thermal debinding step to remove the photopolymer binder [4]. The process is further limited to ceramic powders with low refractive index (predominantly oxide ceramics). Fused filament fabrication (FFF) of ceramics, on the other hand, is a material extrusion method that relies on the continuous deposition of thermoplastic filament. Since it is based on printing of polymers, FFF is well established and of low cost, offering high speed manufacturing and the ability to also produce larger-sized components and multi-material ceramic parts, but at the downside of lower resolution, poorer surface finish when compared to LCM [6].

Despite the advantages AM is offering in terms of shaping of ceramics, sintering remains a crucial and challenging step to consolidate 3D-printed parts. It is a time and energy intensive process, taking place at high temperature to trigger slow solid-state diffusion, densification, pore elimination and grain growth [7,8]. Slow thermal debinding significantly extends the overall processing time. To achieve improved mechanical properties and reliability of (3D-printed) ceramics, dense, fine-grained and homogeneous microstructures are targeted [9]. In order to promote the process of densification, various advanced sintering technologies employing electric field/currents with or without pressure, such as flash, spark plasma sintering (SPS), ultrafast high-temperature sintering (UHS) and cold sintering process (CSP) were developed [10,11]. However, most of them are limited to thin, disk-shaped specimens, especially when mechanical pressure is applied, and thus cannot be fully exploited for sintering of additively manufactured ceramics.

It was previously shown that dry-pressed and colloidally-shaped, as well as additively manufactured ceramics, can be rapidly sintered using pressureless SPS (pSPS) [12,13]. The intense thermal radiation during pSPS provokes rapid heating (250–450°C/min) [14,15] and accelerated

---

[*] Corresponding author.
E-mail address: a.kocjan@ijs.si (A. Kocjan).

[1] Both authors contributed equally to this work.

https://doi.org/10.1016/j.oceram.2026.100981
Received 15 January 2026; Received in revised form 12 May 2026; Accepted 13 May 2026

densification [16], similar to the fast firing (FF) of ceramics [17]. During FF, the green body is immediately subjected to high temperatures, at which grain boundary and lattice diffusion dominate, "skipping" the initial surface-diffusion-controlled particle necking and grain coarsening [18]. In the case of pSPS, the densification acceleration at minimal grain growth was achieved when nanoparticle assembled zirconia green bodies were exposed to rapid radiation, facilitating nanoceramic microstructures through agglomeration, coalescence and sliding of particles in the absence of externally applied pressure and current [13]. In the work of Hofer et al., rapid sintering with pSPS was exploited for LCM-fabricated fine-grained alumina, achieving fast densification without evident grain growth during the intermediate sintering stages. Highly dense and refined microstructures (<500 nm) of LCM-printed, undoped alumina ceramics resulted in improved mechanical strength in comparison to conventionally sintered counterparts [19]. Furthermore, templated grain growth and texturing were achieved in LCM-printed alumina within minutes by the incorporation of alumina platelet seeds [20]. In all mentioned cases, however, the additively manufactured specimens needed to be thermally debinded prior to rapid pSPS sintering, which, in the case of LCM, can last for several days due to extremely slow heating rate and long intermediate dwell times at temperatures <400°C.

More recently, UHS technique, which is likewise based on rapid radiation sintering through a joule-heated carbon felt, realising an order of magnitude faster heating rates than pSPS, was exploited for "immediate" sintering of additively manufactured zirconia parts [21]. Besides densification acceleration, the microstructures were greatly refined with UHS, if nanocrystalline zirconia powders were employed [22]. Moreover, Bhandari et al [23] showed the possibility to combine rapid thermal debinding and sintering, when zirconia parts fabricated via FFF were chemically debinded prior to sintering in order to remove the soluble part of the polymeric binder. The only several-minute-long chemical debinding proved crucial to obtain crack-free printed parts after rapid UHS sintering in only 30 s. The feasibility of rapid thermal debinding and sintering with both UHS and pSPS was further confirmed in alumina specimens fabricated via direct ink writing (DIW) [24]. DIW AM technique has, however, a key advantage since it utilises evaporable solvent and a limited amount of organics prior to the single thermal rapid consolidation step.

While there are clear benefits in using rapid radiation sintering processes such as pSPS and UHS for fast consolidation of (additively manufactured) ceramics, both techniques take place under a reductive environment. Bhandari et al. showed that UHS sintering of alumina [24] and zirconia [23] lead to specimen discolouration due to the presence of remaining graphitised polymer or to a partial oxide reduction at the highest sintering temperatures. Reductive conditions proved more problematic when pSPS and UHS were employed for sintering of functional ceramics such as sodium potassium niobate (KNN) [25] and barium titanate [26], respectively. It resulted in partial reduction and/or phase change, which advocated for post-annealing in air. An additional limitation of the above presented studies is in the manufacturing and rapid sintering of specimens with limited size and geometry, be it with LCM, FFF or DIW. The investigated specimens were of small sizes (≤10 mm), being more or less planar, with relatively big open-like channels (gyroids), thin walls or struts (≤1 mm) in order to promote efficient thermal irradiation and potential removal of organics. Thus, it remains to be seen if rapid sintering approaches, employing high heating rates (≥100°C/min), can also be used for rapid consolidation of substantially larger additively manufactured components, exhibiting thick(er) struts.

The present study aimed to investigate the prospects of rapid radiation sintering, using pSPS set-up, of large-sized complex-shaped alumina geometries by varying the heating rate. Namely, the FFF technique was employed to fabricate tetrahedron geometry with strut thicknesses of 5 mm, where the edge lengths varied from 15 mm to 40 mm. Tetrahedron shape was selected as a model geometry with sufficient shape complexity to investigate the effect of sintering conditions on densification of 3D-printed parts. Thus, the effect of various heating rates (33−300°C/min) and the size of the tetrahedra on the sintering outcome, such as discolouration and (micro)cracking, densification, microstructural evolution (grain sizes) and mechanical properties were studied.

2. Material and methods

2.1. Fused filament fabrication of alumina frameworks

Commercial alumina filament (Zetamix, Nanoe, France) with a diameter of 1.75 mm was used to fabricate tetrahedron frameworks on a HAGE3D 140 L (Hage3D GmbH, Austria) FFF machine. Filament consisted of 45 vol.% of alumina powder dispersed in a polyolefin-based binder system [27]. Tetrahedron shape was selected as a model geometry with sufficient shape complexity. The geometries were designed using Fusion360 (Autodesk, USA) software, where the shape consisted of six connected cylindrical struts with rounded ends (Fig. 1a). The struts of tetrahedron are further labelled as base (bottom, horizontal direction) and lateral (vertical direction) edges, depending on printing and sintering position (Fig. 1a). Simplify3D printing software was used to slice the geometry into layers and determine the printing parameters. (Fig. 1b). Preliminary printing trials were performed using a 0.4-mm-sized nozzle, which resulted in extensive clogging and a non-satisfactory printing outcome. Using a nozzle with a diameter of 0.6 mm eliminated clogging and improved the printing outcome (Fig. 1c).

To avoid breaking of the filament, it was manually fed into the nozzle. The final printing temperature of 125°C was chosen based on preliminary testing of printing temperatures between 120–150°C. The printing bed temperature was set to 30°C. The other printing parameters can be found in Table S1 (Supplementary materials). The size of the tetrahedra was adjusted by changing the length of the struts. As shown in Fig. 1d, three different sizes of tetrahedra were printed, all having an edge thickness (diameter) of 5 mm, whereas the edge lengths were 15, 30 and 40 mm.

2.2. Chemical and thermal debinding

Chemical debinding of printed tetrahedra was performed in acetone in a glass beaker. All of the samples were placed in an upright (printed) position on a metallic mesh for uniform exposure to acetone and then submerged in acetone for 6 h (according to manufacturer recommendations [27]). In addition, ultrasound and shaking at 50 rpm was conducted to promote solvent penetration and polymer dissolution. Following chemical debinding, the frameworks were dried in ambient atmosphere for 2 h. For thermal debinding, the frameworks were placed into alumina crucibles surrounded by γ-alumina powder (Nabalox N201, Nabaltec, Germany) for the wick debinding [28]. Thermal wick debinding was performed in a chamber oven at 600°C for 2 h at a heating rate of 8°C/h. Thermal analysis (TG-DTA) of the as-printed sample was conducted in air, employing heating rate of 5°C/min and final temperature of 650°C, using Jupiter 449 simultaneous thermal analysis instrument (Netzsch, Selb, Germany).

2.3. Rapid radiation sintering – pressureless spark plasma sintering (pSPS)

The rapid radiation sintering (pSPS) in vacuum (≤10 Pa) was conducted in SPS furnace (Dr. Sinter 3000, SPS Syntex Inc., Japan) in a specially designed graphite crucible exerting no pressure or current onto the sample during sintering. The tetrahedra were placed on a 5-mm-thick carbon (C) felt at the bottom of the crucible, which thermally insulated the sample from conductive heat transfer from the bottom (Fig. 2a). The outer walls of the graphite crucible were insulated with carbon felt. The temperature was measured using an infrared pyrometer, where the measuring point was pointed at a small hole on the outer wall

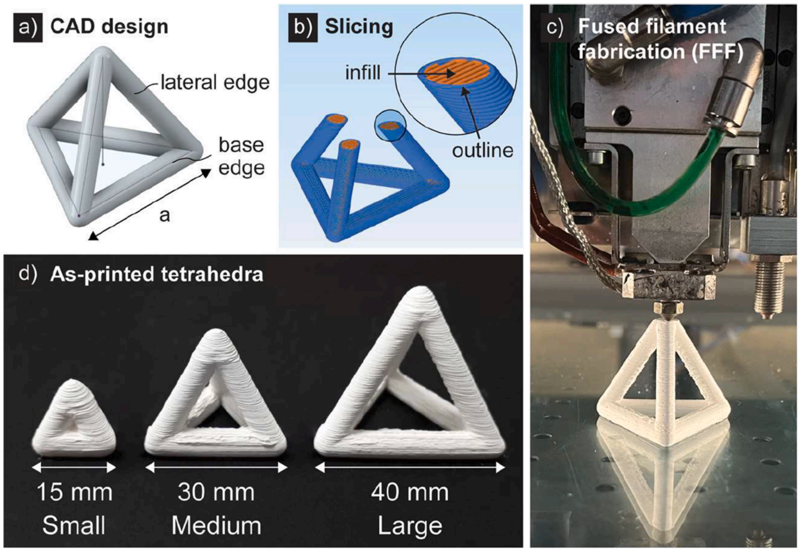

Fig. 1. Fused filament fabrication (FFF) of alumina tetrahedron frameworks. (a) CAD design of the tetrahedron showing base and lateral edge positions. (b) The slicing and the infill strategy for printing of tetrahedron, where blue and orange colours indicate the outline and the infill, respectively. (c) FFF build-up process of tetrahedron on the printing bed. (d) Size comparison between the smallest (S), the medium (M) and the largest (L) as-printed tetrahedra.

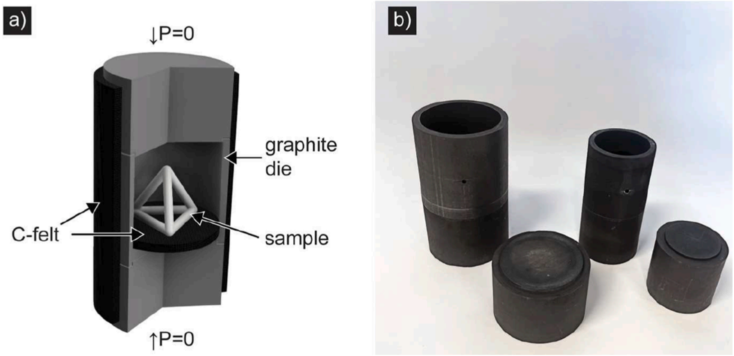

Fig. 2. Pressureless spark plasma sintering (pSPS) set-up. (a) Schematic representation of pSPS graphite set-up showing tetrahedron component placed on the bottom of graphite crucible on 5-mm-thick carbon felt and (b) photograph of the two graphite crucibles used varying the inner diameter (62 mm versus 42 mm) and height (64 mm versus 50 mm) of the crucible.

of the graphite crucible at the height of the sample inside (Fig. 2b). In the pSPS sintering cycle, the temperature was raised to 650°C over a period of 9 min, followed by a given heating rate to reach the set sintering temperature. After dwell time, specimens were cooled down to 600°C over a period of ~20 min. The sintering temperature and dwell time were set to 1550°C and 8 min, respectively, which were sufficient to rapidly sinter LCM-printed alumina samples to full density [19]. Three different heating rates were employed, i.e., 33, 100 and 300°C/min, corresponding to the total sintering times (excluding preheating and cooling) of 35, 17 and 11 min, respectively. Three L tetrahedra were sintered at each heating rate, while only one in the case of M and S tetrahedra.

2.4. *Characterisation of rapidly sintered tetrahedra*

The mass losses of the tetrahedra after debinding were evaluated gravimetrically. The longitudinal dimensions of base and lateral edges (Fig. 1a) in green and sintered states were measured using a digital calliper.

The dilatometric analysis of the printed and thermally debinded test specimen (with a diameter of 6 mm and a height of 6 mm) was conducted in air using optical dilatometer (Misura ODHT, Expert System Solutions S.r.l., Italy) with a heating rate of 33°C/min and a dwell time of 8 min at 1550°C.

The densities of the sintered samples were determined using the Archimedes method, with distilled water as the immersion medium. For the calculation, densities of water and alpha alumina of 0.998 (at 20°C) and 3.987 g/cm^3, respectively, were employed.

For the microstructural analysis, the cross-sections of edges were cut and metallographically polished (to 1 μm finish), followed by thermal etching at 1400°C with a heating rate of 20°C/min and a dwell time of 15 min. Microstructures of the carbon-coated specimen surfaces were analysed using a scanning electron microscope (FEI, HeliosNanolab 650, United States). The grain sizes were analysed using ImageJ software, where the linear intercept technique was employed, measuring at least 250 grains for each sample investigated. No correction factor was applied to the calculation.

X-ray diffraction (XRD) patterns of polished cross-sections of each specimen were recorded over the range 20–30° 2θ using a PANalytical X'pert PRO MPD diffractometer (PANalytical, Almelo, Netherlands) equipped with a PIXcel detector and using a Cu–K1 radiation source.

The hardness measurements were performed on polished sample surfaces utilizing a Vickers diamond indenter (Innovatest, Nexus 7500, Netherlands). Four indentations were made in the core and four were in made on the perimeter of the sample (shell) cross-section. The indentations were made using a force of 5 kg (HV5) with an indentation dwell time of 10 s. For the indentation fracture toughness (K_{ifr}) the and dimensions of the cracks and indentations were measured with optical microscope equipped with corresponding software. K_{ifr} values were calculated according to the empirical derivations of Anstis [29] and Tanaka [30]. Typical indents can be seen in Fig. S2 (Supplementary materials).

3. Results

3.1. Mass loss, shrinkage and density after thermal debinding and sintering

The thermal debinding process resulted in a weight loss of ~23 wt.%, indicating the transition from green body to white body, which was, however, significantly higher compared to the manufacturer's specification (~17 wt.% [27]). After sintering, an additional 2 wt.% of the starting mass was lost. According to TG-DTA conducted on a green sample, presented in Fig. S1 (Supplementary materials), the sample was completely debinded at 530°C with a mass loss from a binder burnout of ~27 wt.%, which corresponds well to the observed mass loss after sintering. The two exothermal DTA peaks at 347°C and 474°C represent the multi-step decomposition of the binder, indicating that a two-component binder is used to produce the filament.

Prior to rapid radiation sintering with pSPS device, the sintering conditions replicated from [19], i.e., 1550°C and 8 min of dwell time, were analysed with optical dilatometer on a printed and debinded test specimen, employing heating rate of 33°C/min (50°C/min is dilatometer limit). As can be seen from Fig. S2 (Supplementary materials), the used conditions resulted in complete densification of alumina specimen. The onset of densification occurred at ~1050°C with maximum densification rate at 1524°C. The total shrinkage in *z*-direction was 21.7%.

The averaged shrinkage of the tetrahedra after rapid pSPS sintering at all heating rates per size are presented in Fig. 3. Large tetrahedra exhibited an edge shrinkage of ~22.8% and ~23.6% for the base (*x*-*y*) and lateral (close to *z*) direction, respectively. A bit more pronounced difference in base versus lateral edge shrinkage was observed in M, i.e., 22.8% and 24.3%, respectively, while base/lateral shrinkages were similar (~23.3%) in the case of S, probably owing to shortest edge distance. According to the filament manufacturer, 20.8% and 23.0% shrinkages are expected in the *x*-*y* and the *z*-direction, respectively [41], which is are slightly lower to the values measured for L and M specimens. It should be noted that the manufacturer's specifications were based on the processing of parts with wall thickness of 2 mm, while in the present case, the initial printed edge thickness was 5 mm.

Measuring all the sintered specimens exhibited a relative density of 96.07 ± 1.49% of theoretical density (TD), which indicates that all specimens were completely densified with pSPS irrespective of the heating rate employed. Specimen densities with respect to their size and heating rates are presented in Fig. 4.

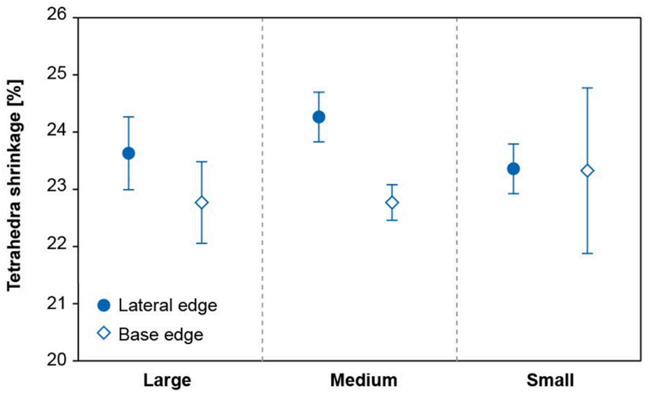

Fig. 3. Average shrinkage values of alumina tetrahedra of various sizes and of various edges (lateral versus base) after rapid pSPS sintering (averaging all heating rates).

In the case of S and M-sized tetrahedra, the slowest heating rate of 33°C/min resulted in the highest relative densities. Increasing the heating rate to 100°C /min resulted in a slight decrease of density, which was then slightly increased with the highest heating rate of 300°C /min, but to a lower value than in the case of 33°C/min. Approximately 3–4% lower TD densities were attained in the S specimens in comparison to M. However, the opposite trend was observed in L specimens. Namely, the highest average relative densities were attained with the heating rate of 100°C /min. Heating rates of 33°C /min and 300°C /min resulted in slightly lower values. Nevertheless, all values are comparable to densities obtained with M-sized specimens, scattered around 97% TD value. The differences become less pronounced when averaging relative densities across all three sizes (300°C /min: 95.12%, 100°C/min: 96.22%, 33°C/min: 95.65%).

3.2. Rapid sintering related cracking and discolouration of tetrahedra

After pSPS sintering the samples were cooled down in the graphite crucible and, owing to the reductive environment, the samples exhibited greyish colour, as can be seen in Fig. 5a, representing typical L specimen. In addition, a small microcrack at the upper corner extending radially into the lateral edge can be also observed. Inspecting the cross-sections revealed complex interior crack systems. In the case of lateral edge, the crack was initiated in the edge centre and propagated, branched into three (Fig. 5b) or only two radial directions (Fig. S3; Supplementary materials), being arrested within the edge core. In the case of base edge (Fig. 5c), besides the cracks present in the core of the edge, there are cracks that were initiated at the outer edge perimeter extending into the core. Some of these outer cracks could also connect to the inner branched crack system and were predominantly present in the lower half of the base edge (Fig. S3; Supplementary materials).

Apparently, these outer cracks were initiated from the printing defects, occurring at the lower half of the base edges of the tetrahedra, as presented in the close-up Fig. 5d These voids were formed at the junction of the outline and infill intersections (where the orange and blue lines meet in Fig. 1b). The lateral edges were free of these types of defects. It is important to note that the extensive microcracking of the edges was only observed in the largest L specimens, whereas M and S tetrahedra were defect free (Fig. S4; Supplementary materials).

In general, the base edges were more extensively discoloured, whereas the discolouration was heterogeneous but consistent for all of the samples (Figs. S3–4; Supplementary materials). Namely, samples exhibited a thin bands: *i*) an outer grey was followed by *ii*) an inner white band, optionally followed by *iii*) the thicker inner semicircle. The thicknesses of the observed bands were assessed only for the L and M tetrahedra, since these exhibited a pronounced edge length (Fig. 1d). It can be observed that both outer and inner bands have similar thicknesses of several tens of micrometres (~50–100 μm), with the notable decreases in thickness with the increase of heating rate (Fig. S5; Supplementary materials). The polished cross-sections of L tetrahedra were analysed with XRD for determining the phase composition (Fig. S6; Supplementary materials), exhibiting alpha alumina characteristic peaks (according to JCPDS-ICDD file no.46–1212).

3.3. Microstructural evolution

SEM micrographs for L tetrahedra sintered at different heating rates are presented in Fig. 6. For comparison conventionally sintered specimen (1550°C with a 2 h dwell time) is included as well (Fig. 6a). The microstructure conventionally sintered sample is composed of polygonal grains, typical for alumina, where some of the grains tend to elongate (indicating templated grain growth). The latter could be ascribed to the initiation of exaggerated grain growth. A substantial amount of residual porosity was observed as well.

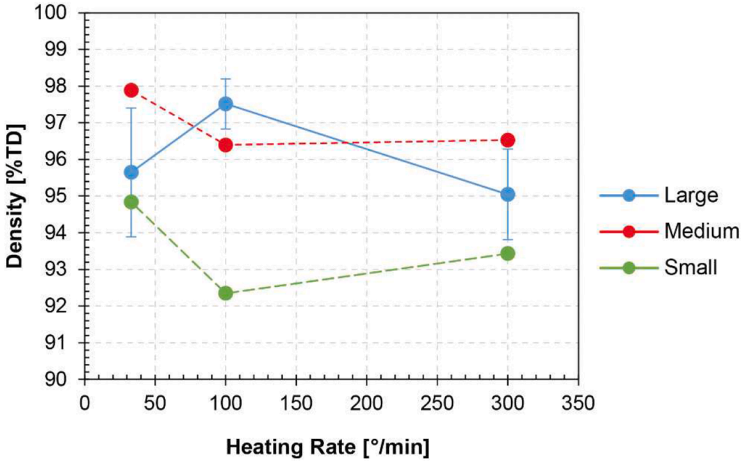

Fig. 4. Relative densities of alumina tetrahedra of various sizes with respect to the heating rate.

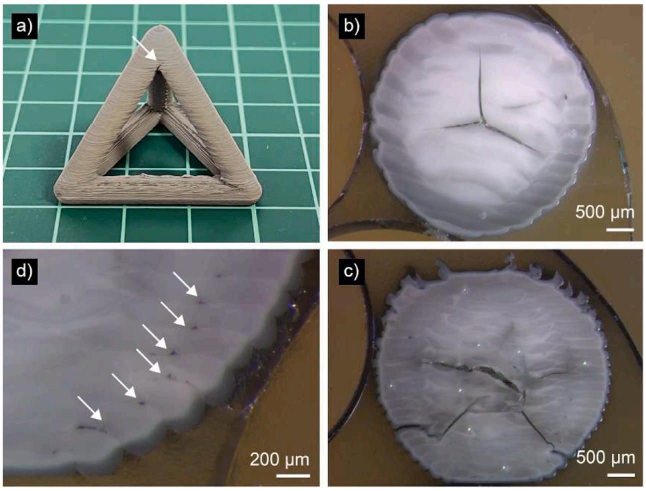

Fig. 5. Alumina tetrahedra after rapid sintering. (a) The typical grey colour exhibited by one of the large sintered tetrahedron. Notice the small microcrack at the upper corner extending radially into the lateral edge. Polished cross-sections revealed interior crack systems in the (b) lateral and (c) base edges of tetrahedron, where (d) is the close-up of the lower the lower half of the base edge.

In contrast, microstructures of L specimens (Fig. 6b-d) were completely dense and consisted of equiaxed grains (no elongation), even if the sintering temperature of the specimen and the sintering dwell time 15-times shorter.

In terms of grain size and morphology, the difference between L specimens sintered at various heating rates was not significant. In contrast to the conventionally sintered samples, which had the largest grain size (at the lowest relative density), L specimens exhibited similar grain sizes across all three heating rates, with the 100°C/min being the smallest. However, slight differences in the residual porosity can be observed with the increase in the heating rate. Bigger pore agglomerates were observed in the triple junctions for the L specimen sintered with 33°C/min (Fig. 6b). On the other hand, with increased heating rate (≥100°C/min), several smaller pores were observed, few trapped within grains (Fig. 6c-d).(Table 1).

The S specimens rapidly sintered at 100°C/min exhibited the smallest grain sizes, as seen from Fig. 7. It can also be seen that this specimen contains considerable amount of residual porosity, corroborating with the lower measured relative densities (Fig. 4). The remaining pores were conglomerated to isolated areas, with already visible intraparticle porosity, but also pores pinning two grain boundaries.

Given the observed discoloration differing with the edge position (base versus lateral and core versus shell) in the tetrahedron framework and heating rate, especially in the L specimens, the grain sizes were also assessed with respect to these positions and are presented in Fig. 8. It can be observed that grain size was always larger in the outer shell compared to the core of the tetrahedra edges. In addition, grain sizes are generally smaller on the base edges compared to lateral ones. Grain sizes for the shell region of the lateral edge were decreased with increased heating rate, while for the core region of L specimen sintered with 100°C/min exhibited the smallest grain sizes. The latter correlation can be applied for both shell and core base edges.

3.4. Mechanical properties

Vickers hardness was evaluated for the L specimens at different tetrahedron positions for all three heating rates (Fig. 9). Even though the shell possessed higher grain sizes (Fig. 8), the hardness of the shell regions was always slightly higher compared to the core irrespective of the heating rate employed.

In general, the L specimens sintered at 100°C/min have the highest hardness, with an average of 18.5 GPa. L specimens sintered at 33 and 300°C/min have comparable hardness, i.e., 17.9 GPa and 17.8 GPa, but the differences were not significant. However, even though showing lower hardness values, the L specimens sintered at 33°C/min exhibited a more pronounced scatter of values compared to the one at 300°C/min. On the other hand, the base edges show a higher hardness than the lateral edges, which corresponds to the smaller grain sizes measured in the base edges (Fig. 8). The average hardness of different tetrahedron sizes across all three heating rates is comparable between medium and large tetrahedra (~19 GPa), but noticeably lower for small tetrahedra (~16 GPa) (not shown), which can be ascribed to the observed residual porosity present in the small tetrahedra (Fig. 7).

The indentation fracture toughness was evaluated for L specimens and was found to be higher in the core compared to the shell area. This was ascribed to the presence of residual porosity within the core area, where the residual pores can deflect or arrest the propagating crack, slightly increasing the resistance to fracture. On the other hand, differences between base and lateral edges, between the three heating rates and between the sample sizes are not significant according to either empirical method employed.(Table 2).

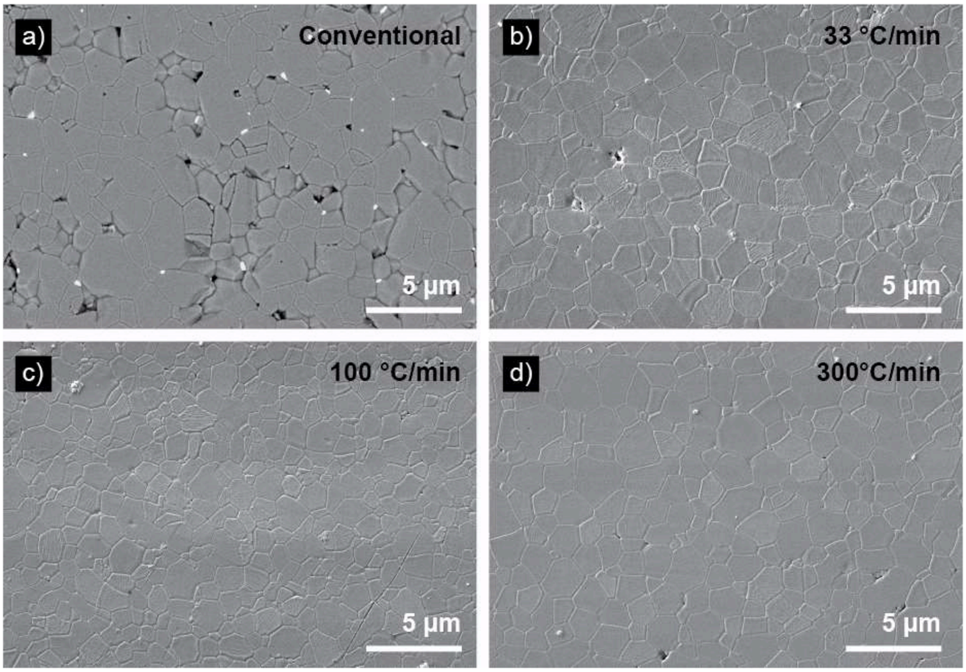

Fig. 6. Microstructural evolution. SEM analysis of thermally etched cross-section for the (a) conventionally sintered specimen and for the L tetrahedra sintered at (b) 33°C/min, (c) 100°C/min, and (d) 300°C/min heating rate.

Table 1
Average grain size for the rapidly sintered L specimen compared to the conventionally sintered specimen was calculated with the linear intercept method.

Sample	Sintering regime	Grain size (µm)
CS	1550°C, 2 h, 3°C/min	1.41 ± 0.14
pSPS L33	1550°C, 8 min, 33°C/min	1.31 ± 0.16
pSPS L100	1550°C, 8 min, 100°C/min	1.08 ± 0.13
pSPS L300	1550°C, 8 min, 300°C/min	1.23 ± 0.17

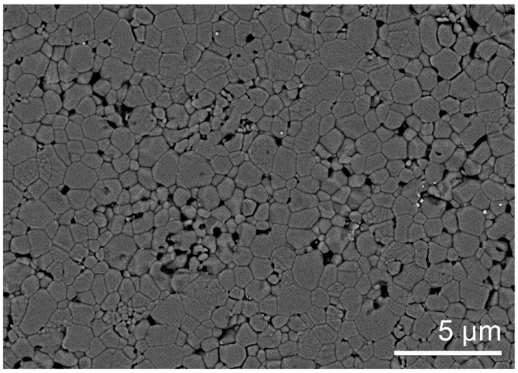

Fig. 7. SEM micrograph of thermally etched cross-section of the smallest S tetrahedron rapidly sintered at 100°C/min.

4. Discussion

4.1. *Extrusion-based fabrication of large alumina objects subjected to rapid sintering*

The FFF method forms layers by fusing the extruded filament on the print bed, which flattens from circular to ellipsoidal shape. As a consequence, the filament fusion within a single layer (*x-y*, horizontal plane) can be stronger and denser than between layers (*z*, vertical printing direction), due to the lower inter-filament, freshly bonded surface area [31,32]. The higher fusion area in the *z*-axis can likely lead to imperfections, such as porosity and voids, especially in the large-sized objects with increased number of layers. Consequently, anisotropy in shrinkage during sintering can be expected and will be more pronounced in the vertical, *z*-direction, as the interlayer voids are eliminated which results in greater shrinkage upon sintering [33,34].

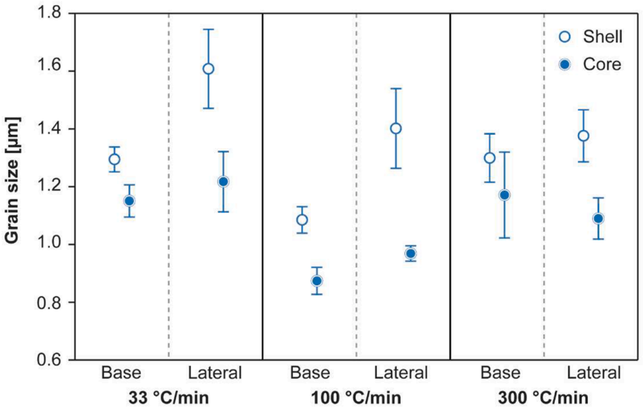

Fig. 8. Grain sizes for base and lateral edges at the core and shell cross-sectional positions of L specimens with respect to the different heating rates.

Here, the shrinkage in the *z*-direction corroborated to the one provided by the manufacturer [27]. The shrinkage of the lateral edge was larger than the shrinkage of the base edge, especially in the L and M specimens with longer edge lengths (Fig. 3). Similarly, in the work of Tosto et al [35], where alumina filament of the same manufacturer was used, however, with higher solid loading (52 vol%), shrinkage in *x-y* and *z* direction for the printed 10-milimetre-sized cubes differed and was 20.7% and 22.9%, respectively. Even more pronounced shrinkage anisotropy was observed by Gorjan et al [36], i.e., 17% and 23% in *x-y* and *z*-direction, respectively, but for printing of a planar, disk-type of specimens (1 mm thick and 20 mm in diameter) with a

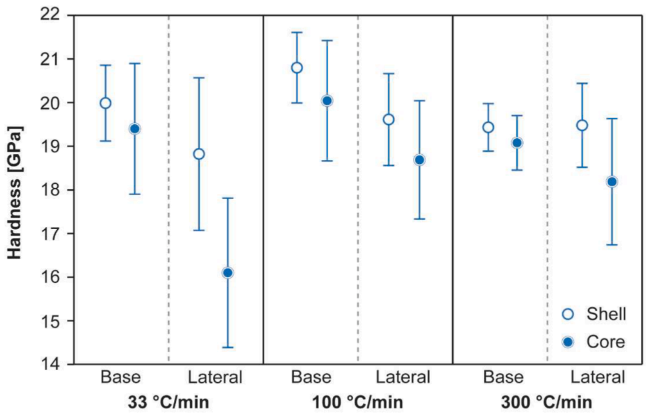

Fig. 9. Vickers hardness at for the L tetrahedra in respect to the position of the framework (shell versus core in base and lateral edges) as a function of heating rate. Five measurements per position are presented, where average hardness is shown with translucent marker and standard deviation.

Table 2
Indentation fracture toughness for the L tetrahedra in respect to the position of the framework (shell versus core in base and lateral edges) averaging all heating rates.

Indentation fracture toughness (K_{ifr}):	Tanaka (MPa·m$^{1/2}$)	Anstis (MPa·m$^{1/2}$)
Lateral edge	3.07 ± 0.68	2.94 ± 0.67
Base edge	3.21 ± 0.77	2.94 ±0.53
Shell	2.98 ± 0.43	2.75 ± 0.34
Core	3.29 ± 0.59	3.13 ± 0.42

custom-developed binder formulation for the 50 vol% alumina containing filament. Thus, the slightly higher shrinkages observed here can be related to the lower alumina solid loading in the filament contributing to lower green densities.

The FFF related filament fusion in horizontal, *x-y* direction also resulted in the formation of printing voids (Fig. 5d), which were only present at the lower halves of the base edges. These printing voids can be regarded as defects due to printing [37] that are primarily attributable to high overhang angle and the absence of support material during fabrication (Fig. 1d). As the outline was deposited before the infill in each layer (Fig. 1b), as unsupported overhang, it led to downward sagging under gravitational forces and/or incomplete fusion with the infill, resulting in the observed printing voids. Such printing defects were classified as sub-perimeter voids by Tao et al [38]. In the lateral edges, on the other hand, the outline is also deposited as overhang, but at a lower inclination angle. The formation of sub-perimeter voids explains why the lateral and base edges of largest L specimens exhibited different typical crack systems within the core after sintering. These voids were deleterious for the base edges, since the inner cracks propagated out, whereas microcracks at the lateral edges remain confined in the core (Figs. 5b-c).

The origin of such cracking was ascribed to inhomogeneous densification and shrinkage during rapid sintering [39,40], as evidenced from significantly differing grain size between the core and the shell areas (Fig. 8). Because the outer surface is exposed to higher radiative heat flux during pSPS process, it reaches the sintering temperature sooner, accelerating densification and grain growth in the outer layer [41]. The later processes are faster than the propagation of heat by thermal conduction into the bulk. As a result of thermal gradient and differential shrinkage/densification may occur [39,42,43]. The resultant inhomogeneous densification generates micro-residual stresses [39], i.e., compressive stresses in the shell and tensile stresses in the core, that in present case in L specimens led to cracking of the core of the lateral edges. Moreover, since the shrinkage of the lateral edges was larger than the base edges (Fig. 3), the later evolved tensile stresses, acting on the sub-perimeter voids, ensuring a more extensive cracking of the lower halves of base edges (Fig. 5c). Microcracking was most prevalent at a heating rate of 300°C/min, and occurred almost exclusively in the largest L specimens (Fig. S3; Supplementary materials), with the longest edge lengths (Fig. 1d).

4.2. *Microstructural inhomogeneities as a result of thermal gradient evolution in rapid radiation pSPS sintering*

In the present work, the increased heating rate did not result in a refined microstructure. While it was shown heating rate can accelerate densification at minimal grain growth, but when the initial particle size in the green body was very fine (or even in the nanoscale) [13,19,22,44,45].It follows that the size of starting powder particles dispersed in the polymer (of the commercial filament) is important. If the starting particles are relatively large, the densification potential (at limited coarsening/grain growth) is limited. In the article by Tosto C. et al [35] the Nanoe Zetamix filament was used as well, and the investigation of the initial particle size of the ceramic filler was measured to be 0.91 ± 0.08 µm. The particle size of the filament was re-examined here as well, measured on the ashes of calcined in air (burned-out) filament. It was confimed that the mean particle size was indeed around ~1 µm (Fig. S7; Supplementary materials). This further suggests that initial particle size dominated the final grain size, limiting the benefits of increased heating rates for microstructural refinement. Nevertheless, the rapid radiation sintering did substantially improve densification, as can be clearly observed form higher shrinkage values when compared to the linear shrinkage of the dilatometric analysis (Fig. S7; Supplementary materials) and to the manufacturer ones [27]. In addition, microstructures of rapidly heated samples were denser (with slight grain size refinement) when compared to conventional sintering of the same material (Fig. 6), where the observed intraparticle porosity (Fig. 6c-d) can be regarded as a direct consequence of accelerated densification due to pronounced grain boundary and lattice diffusion processes.

A noticeable difference between grain sizes was observed here between the core-shell regions as well as in lateral and base edges (Fig. 8). The differences corroborate with the observed microcracking originating from the possible inhomogeneous densification and shrinkage owing to the obvious evolution of thermal gradients within frameworks during rapid radiation sintering. To better understand the eventual temperature gradients in the frameworks, finite elements (FE) simulation was used (for simulation details please refer to the Appendix) to simulate the temperature evolution in the pSPS set-up (Fig. 10a). From the evolution of average FEM simulated temperature of the specimen during pSPS with 33°C/min and 300°C/min (Fig. S8; Supplementary materials), it can be observed that the specimen temperature aligns with the one measured on the crucible in slowest heating rate, while in the fastest, the isothermal conditions during dwell are not met, i.e., the temperature slowly increases. In both cases, there is a difference between the measured temperature of the crucible and of the specimen position, i.e., the centre of the lateral and the base edge reach substantially lower temperatures of ~1500°C and 1440°C, respectively. Visualising the temperature distribution in L and S tetrahedra sintered at 300°C/min at the end of 8-minute-long dwell time (1000 s) (Figs. 10 b-c), the temperature differences between base and lateral edges as well as the L and S specimen are confirmed. The top of the both tetrahedra has slightly lower temperature as-well.

The highest radiostity inside the sintering graphite crucible is at the central part of the side walls, where the temperature is the highest (Fig. 10). Similar observation was already reported by Li, where the top and bottom of the die were consistently cooler than the walls, regardless of the size of the die [14]. It is because the view factor, the fraction of radiation leaving the radiator surface (i.e., die walls) intercepted by the irradiated surface (i.e., sample), is lower for the base edge in comparison to lateral edge, due to its perpendicular position with respect to the walls

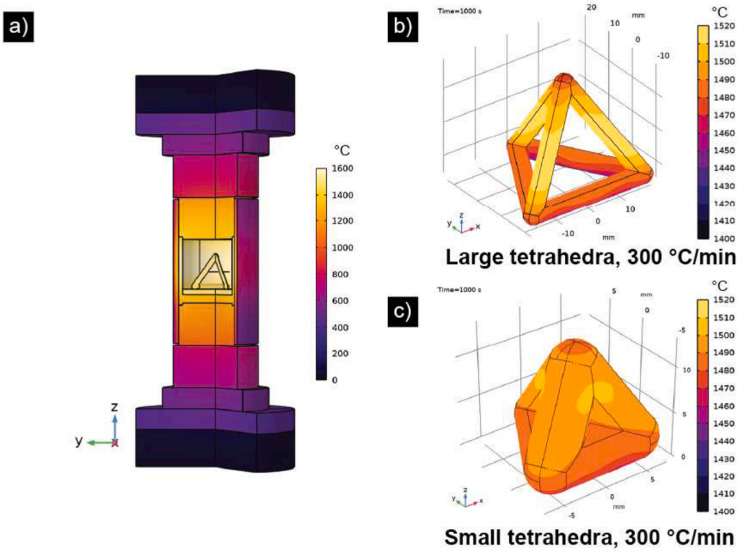

Fig. 10. Finite element (FE) simulation results depicting the temperature distribution in a) the pSPS setup, b) large and c) small tetrahedron sintered with a heating rate of 300°C/min, evaluated at the end of dwell (t=1000 s).

of the die [46]. Furthermore, the presence of the carbon felt underneath the specimen (Fig. 2a) prevents radiative heating of the sample from the bottom side of the die. It follows that the base edge is less exposed to the radiation heat flux from the walls of the radiating die.

In Fig. 11, FE simulated temperature distribution depicted on radial cut planes of the lateral edges for both L and S tetrahedra are presented, showing evolved in-plane thermal gradients as well. It has to be noted, that the actual temperature difference between the surface and the inner part of the samples was most likely significantly higher since homogeneous thermal properties were used for the simulation and do not account for the changes in porosity and thermal properties with densification. Nevertheless, the difference in temperature between the irradiate shell and the shielded core is evident. As a consequence of evolved thermal gradients, the grains near the surface, i.e., in the shell region, exhibit coarser grain sizes compared to the core with slightly lower temperatures. The same analogy goes for the grain size difference between the lateral and base edges. Indeed, the base edges with finer grain sizes exhibit higher hardness than the lateral edges (Fig. 9), corroborating the Hall-Petch effect.

The smallest (S) tetrahedra exhibit much smaller grain sizes and lower overall density (lowering hardness values) compared to the M and L specimens (Figs. 8–9). Lower FE simulated specimen temperature were obtained (Figs. 10–11). One of the reasons could be related to differences in distances of specimens and graphite crucible/radiator walls. Namely, for the L/M and S tetrahedra, sintered in graphite crucible with inner diameters of 62 mm and 42 mm, the specimen bottom corner distance-to-wall was approximately 22 mm and 27 mm, respectively. It was shown that as the distance between radiator and the surfaces of the sample becomes shorter, the view factor increases resulting in an increased amount of radiation energy transfer [14,50]. In addition, due to the reduced size, the S specimen was much "bulkier" (Fig. 1d), thus, the inner edge surfaces of the smaller tetrahedra were not exposed to

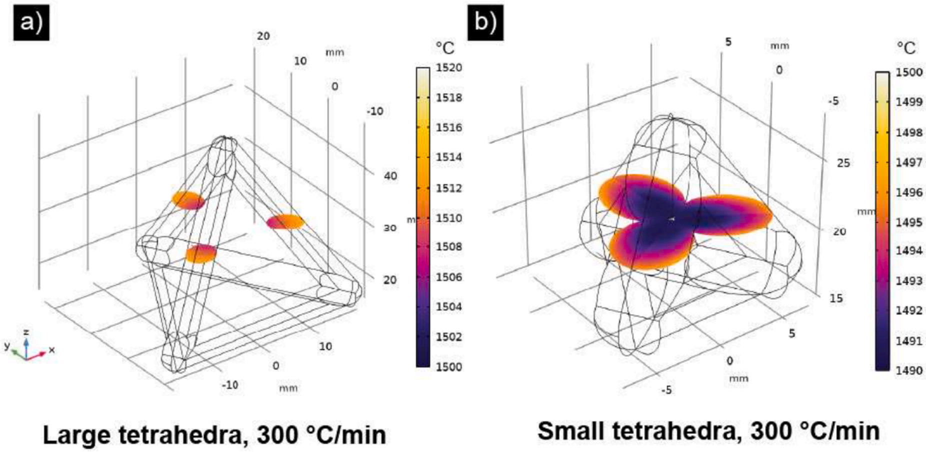

Fig. 11. FE simulated temperature distribution depicted on a cut plane at half height of the tetrahedra for a) large tetrahedra, b) small tetrahedra evaluated at the end of dwell time (t=1000 s). However, the shell regions exhibit higher hardness than the cores of the samples (Fig. 9). Generally, finer grain sizes lead to higher hardness due to the Hall-Petch effect [47]. This decrease in hardness could be explained by the temperature-gradient-mediated anisotropy in shrinkage (Fig. 3), facilitating enhanced densification and compressive stresses that occur in the shell region, which can enhance hardness. Such anisotropy was also shown by García and Hotza [48], when fast firing alumina samples, where a denser outer layer was formed in the sample with relatively porous inner region. The core versus shell comparison was also the only one to yield a statistically significant difference in fracture toughness, with the core regions demonstrating slightly higher toughness. While the shell is harder, it can be also more brittle, likely due to a coarser microstructure, whereas finer grain size in the core and presence of small pores (Fig. 6c) that can deflect the crack [49], contributed to increased indentation toughness by better resistance to crack propagation.

radiation at all. Therefore, the surface area contributing to radiative heat transfer was significantly lower than in the case of M and L specimens.

4.3. Reductive environment of the rapid radiation sintering (pSPS)

A greyish discolouration is a common challenge in SPS sintering [51]. The discolouration of the cross-section observed under the optical microscope (Fig. 5b-c and Figs. S3–4; Supplementary materials) did not show a correlation to heating rate, while it can be concluded that base edges were darker than the lateral ones. Likewise, M/L specimens were darker than S ones. Firstly, discoloration can be ascribed to sintering in a low-oxygen environment under vacuum ($\leq$10 Pa), as is the case for pSPS system, can promote the reduction of the oxide and formation of oxygen vacancies, which act as point defects and may contribute to colour changes. And secondly, evaporation of the carbon phases from the graphite tooling (or polymeric residues from debinding) that is used in both SPS and pSPS can lead to carbon contamination resulting in grey or black discoloration of the oxide.

Discolouration of oxide ceramics after SPS processing has often been reported, especially detrimental for transparent and translucent ceramics [52,53], but also for alumina. In the work of Jiang et al. optically transparent alumina was produced by SPS and the results showed that by increasing the sintering temperature or dwell time, the colour of the disk became darker [51]. The work of Morita et al [54], where the SPS was used to sinter $MgAl_2O_4$ spinel, also showed that heating rates, influence the sample discolouration. However, the samples sintered with slower heating rates (10°C/min) showed only a slight discolouration, which was localized on the specimen surface (300–500 µm). When a higher heating rate (100°C/min) was used, the discolouration affected the entire volume of the 3-mm-thick disc-shaped specimen. Morita et al [55], also investigated alumina, concluding the specimen discoloration was due to carbon contamination during the intermediate stage of sintering through the open pore channels, residing close to the surface region (~75 µm). Apparently, the evaporated carbon penetrated into the specimens through pores, where captured with the pore closure. Interestingly, the carbon contamination was limited to alumina as opposed to spinel. Since densification occurred at a lower temperature in alumina than in spinel, the transition from open to closed porosity at the verge of the final sintering stage occurred at a lower temperature, at which there is less time and lower amount of generated gaseous carbon to penetrate into the deeper parts of the specimen, thus, localising the contamination nearer to the specimen surface.

The thickness of the outer grey layers in the tetrahedra samples presented here (Fig. S5; Supplementary materials) is similar to the ones observed by Morita et al [55] Namely, the outer gray band measured thicknesses were in the range 40–90 µm. In addition, the entire cross-section areas appeared greyish (Fig. 5b-d). If carbon contamination relies on open pore networks for penetration, a plausible explanation would be that the penetration occurred through the inter-filament and inter-layer regions and/or through voids, where pores could be eliminated later and at higher temperature than in the filament itself. Since the base edges were in intimate contact with carbon felt, the discolouring was more pronounced than in lateral ones. In the case of S specimens of lower density, on the other hand, the pores were not closed yet, thus the discolouring was not as severe.

Additional mechanism for discoloration, as already mentioned, would be in formation of oxygen vacancies which serve as light scattering sources [56]. Since pSPS operates in vacuum, oxygen removal from the alumina lattice is thermodynamically favourable. In addition, at temperatures higher than >1600°C and at low oxygen partial pressures, alumina can form gaseous compounds and contact with graphite can also reduce alumina to volatile suboxides [57]. Bhandari et al [58] suggested a possibility of carbothermal reduction of alumina, where carbon originates from the binder burnout during pSPS or UHS. Here, the carbon would have to come from the die, or carbon felt from the bottom, since TG-DTA (Fig. S1; Supplementary materials) suggests a complete binder burnout. In any case, while the part of the specimens turned white after annealing in air at 1400°C for 15 min, as the sample re-oxidized (Fig. S9; Supplementary materials), additional future analytical investigation will be required to confirm the mechanism of discoloration in the rapid pSPS process of thermally debinded additively manufactured alumina ceramics.

5. Conclusions

The present study investigated the prospects of rapid radiation sintering with pSPS of large-sized complex-shaped alumina tetrahedra, fabricated by the FFF AM method, with strut thicknesses of 5 mm, where the edge lengths varied from 15 mm to 40 mm.

All tetrahedra sizes survived the rapid sintering. Irrespective of the heating rate employed (33–300°C/min) medium (M) and large (L) specimens exhibited a relatively high density ($\geq$96%), while smaller (S) specimens were slightly less dense (92–95%) due to the lower temperatures achieved.

The increased heating rate did not refine the microstructures due to the relatively large size of initial powder particles (~1 µm) present in the commercial filament. However, accelerated densification was still observed, as indicated by higher shrinkage, finer and denser microstructures, as compared to the conventional sintering in air.

The pSPS reductive environment have led to discoloration of the samples, where the base edges in contact with the carbon felt were more prone to discolouration than the lateral one. The interfilament layers potentially served as path for carbon penetration.

The rapid radiation sintering at present conditions (1550°C, 8 min) contributed to the evolution of thermal gradients, as simulated by FE, that further affected the sintering outcome, i.e., to the inhomogeneous shrinkage, densification and microstructural evolution with respect to the edge position (base versus lateral edge and core versus shell edge area). As a consequence, grain size and mechanical properties were highly sensitive to the tetrahedron point of inspection. The anisotropy in shrinkage and differential densification were responsible for microcracking of the largest (L) tetrahedra (with edge length of 40 mm), while the smaller tetrahedra, M and S, were crack-free.

In summary, rapid radiation sintering, such as pSPS, can be exploited for sintering large (alumina) ceramic components, but inhomogeneous thermal distribution during rapid sintering can (negatively) affect the homogeneous shrinkage and densification. Possible mitigation approaches for minimising thermal gradients would be employing much finer initial particle sizes, designed thinner-walled structures and/or increasing the sample surface exposed to heating element radiosity at the bottom component surfaces by using support structures instead of carbon felt.

CRediT authorship contribution statement

Aljaž Iveković: Writing – review & editing, Writing – original draft, Supervision, Methodology, Conceptualization. **Miha Križaj:** Writing – original draft, Validation, Methodology, Investigation, Formal analysis, Data curation, Conceptualization. **Andraž Kocjan:** Writing – review & editing, Writing – original draft, Supervision, Resources, Project administration, Methodology, Conceptualization.

Declaration of competing interest

The authors declare that they have no known competing financial interests or personal relationships that could have appeared to influence the work reported in this paper.

The author is an Editorial Board Member/Editor-in-Chief/Associate Editor/Guest Editor for [*Journal of the European Ceramic Society]* and was not involved in the editorial review or the decision to publish this article.

Andraž Kocjan

Acknowledgements

This work was supported by the Slovenian Research Agency funding research project and program N2-0301 and P2-0087, respectively. The authors would like to thank Aleksander Učakar for assisting with scanning electron microscopy.

Supplementary materials

Supplementary material associated with this article can be found, in the online version, at doi:10.1016/j.oceram.2026.100981.

Appendix

3D model of pressure-less spark plasma (pSPS) sintering furnace configuration (Fig. 1a) was developed utilising COMSOL Multiphysics software. To reduce the time and processing intensity of the model, sector symmetry was employed using a representative 120° section of the simulation geometry. To increase the simulation accuracy, the mesh was refined in the sample domain.

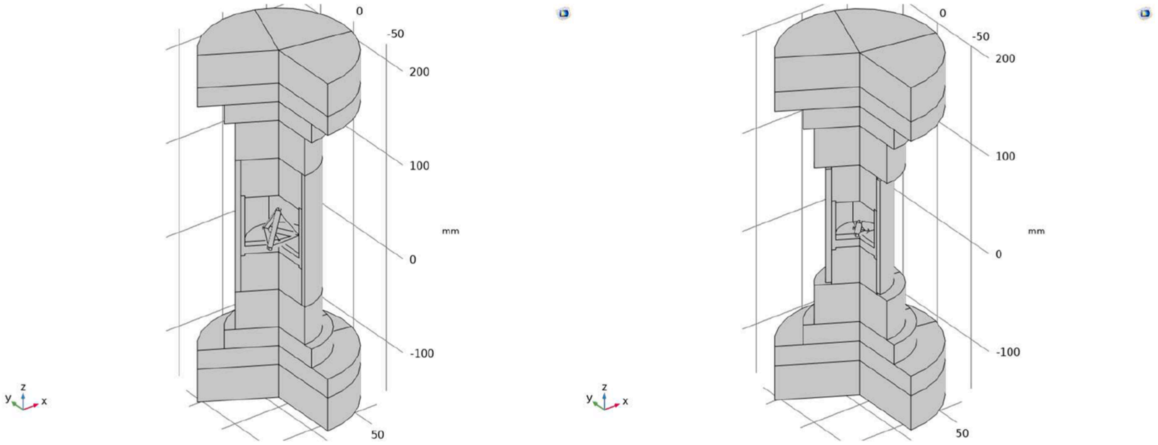

Fig. 1a. 3D pSPS column geometry used in the simulation with a large (left) and small tetrahedron (right) represented with two sectors. For illustrative purposes, the full tetrahedra geometry is displayed.

To reduce the unnecessary complexity of the model, several assumptions and initial boundary conditions were applied. As the sintering was conducted in a vacuum, the heat losses by conduction or convection through gas were neglected. The sample was assumed to be homogeneous in terms of its bulk thermal and electrical properties. Literature values for (temperature-dependent) properties of Inconel, graphite, and alumina, and properties of the graphite felt provided by the manufacturer, were used for the calculation and are presented Table 1.Table 1a.

Table 1a
Physical properties of materials used in the FE calculations (with T in Kelvin) [59].

	Inconel	Graphite	Graphite felt [60]	Al_2O_3 [61]
Heat Capacity, Cp (Jkg-1K-1)	$344 + 2.5 \times 10^{-1}T$	$34.27+2.72 \times T-9.60 \times 10^{-4}T^2$	200	850
Thermal conductivity, k (Wm-1K-1)	$10.09 + 1.57 \times 10^{-2}T$	$82.85–0.06•T + 2.58 \times 10^{-5}T^2$	$0.0061+8 \times 10^{-5}T - 1 \times 10^{-7}T^2 + 8 \times 10^{-11}T^3$	$39\,500\ T^{-1.26}$
Electrical resistivity ρe (Ωm)	$9.82 \times 10^{-7}+1.6 \times 10^{-10}T$	$2.14 \times 10^{-5} - 1.34 \times 10^{-8}T + 4.42 \times 10^{-12}T^2$	0.01	$8.7 \times 10^{19}\ T^{-4.82}$
Density, ρ (kgm-3)	8430	1904–0.01414T	120	3899
Emissivity, ε	0.67	0.8	0.99	0.65 [62]

Concerning the heat flux, limit conditions have been imposed on the outer vertical and horizontal boundaries: A radiative heat flux was assumed on all the outer vertical walls of electrodes, spacers, die, and punches, with surface emissivity values depending on the material (see Table 1) and the ambient temperature set at 300 K. A convective heat flux (heat transfer coefficient h_c=200 W/(m^2K), constant water temperature of 300 K was assumed for the electrode surfaces in contact with the cooling system. Electrical and thermal contact resistance at the electrode-spacer and spacer-spacer interfaces was used to calibrate the simulation to obtain a good fit between the simulated and experimentally measured temperature values.

References

[1] A. Zocca, P. Colombo, C.M. Gomes, J. Günster, Additive manufacturing of ceramics: issues, potentialities, and opportunities, J. Am. Ceram. Soc. 98 (2015) 1983–2001, https://doi.org/10.1111/jace.13700.

[2] U. Scheithauer, R. Johne, L. Gottlieb, S. Weingarten, H. Wiemer, S. Holtzhausen, Recent developments in the field of additive manufacturing of ceramic-based multi-material components open the door to highly functionalized components, Prog. Addit. Manuf. 10 (2025) 4051–4059, https://doi.org/10.1007/s40964-025-01112-6.

[3] T.D. Ngo, A. Kashani, G. Imbalzano, K.T.Q. Nguyen, D. Hui, Additive manufacturing (3D printing): A review of materials, methods, applications and challenges, Compos. B Eng. 143 (2018) 172–196, https://doi.org/10.1016/j.compositesb.2018.02.012.

[4] S. Zakeri, M. Vippola, E. Levänen, A comprehensive review of the photopolymerization of ceramic resins used in stereolithography, Addit. Manuf. 35 (2020) 101177, https://doi.org/10.1016/j.addma.2020.101177.

[5] M. Schwentenwein, J. Homa, Additive manufacturing of dense alumina ceramics, Int. J. Appl. Ceram. Technol. 12 (2015) 1–7, https://doi.org/10.1111/ijac.12319.

[6] I. Özden, A. Iveković, A. Kocjan, Additive manufacturing of ceramics from thermoplastic feedstocks, Open Ceram. 6 (2021) 100129, https://doi.org/10.1016/j.oceram.2021.100129.

[7] Y.-M. Chiang, D.P. Birnie, W.D. Kingery, Physical Ceramics: Principles for Ceramic Science and Engineering, John Wiley & Sons, Inc., 1997.

[8] F. Lange, Powder processing science and technology for increased reliability, J. Am. Ceram. Soc. 72 (1989) 3–15. http://onlinelibrary.wiley.com/doi/10.1111/j.1151-2916.1989.tb05945.x/abstract. accessed January 27, 2013.

[9] G.L. Messing, A.J. Stevenson, Toward pore-free ceramics, Science 322 (2008) (1979) 383–384.

[10] M. Biesuz, S. Grasso, V.M. Sglavo, What's new in ceramics sintering? A short report on the latest trends and future prospects, Curr. Opin. Solid State Mater. Sci. 24 (2020) 100868, https://doi.org/10.1016/j.cossms.2020.100868.

[11] D. Sohrabi Baba Heidary, M. Lanagan, C.A. Randall, Contrasting energy efficiency in various ceramic sintering processes, J. Eur. Ceram. Soc. 38 (2018) 1018–1029, https://doi.org/10.1016/j.jeurceramsoc.2017.10.015.

[12] D. Salamon, Z. Shen, Pressure-less spark plasma sintering of alumina, Mater. Sci. Eng. A 475 (2008) 105–107, https://doi.org/10.1016/j.msea.2007.01.162.

[13] A. Kocjan, M. Logar, Z. Shen, The agglomeration, coalescence and sliding of nanoparticles, leading to the rapid sintering of zirconia nanoceramics, Sci. Rep. 7 (2017) 1–8, https://doi.org/10.1038/s41598-017-02760-7.

[14] D. Li, Rapid sintering of ceramics by intense thermal radiation, Doctoral thesis, Stockholm University, Faculty of Science, 2016.

[15] A. Kocjan, N. Bhootpur, A. Iveković, M. Eriksson, Rapid densification of nanocrystalline zirconia: pressureless versus pressure-assisted spark plasma sintering, Open Ceram. 19 (2024) 100657, https://doi.org/10.1016/j.oceram.2024.100657.

[16] D. Salamon, K. MacA, Z. Shen, Rapid sintering of crack-free zirconia ceramics by pressure-less spark plasma sintering, Scr. Mater. 66 (2012) 899–902, https://doi.org/10.1016/j.scriptamat.2012.02.013.

[17] M. Harmer, E. Roberts, R. Brook, Rapid sintering of pure and doped alpha-Al2O3, Trans. J. Br. Ceram. Soc. 78 (1979) 22–25.

[18] M. Harmer, R. Brook, Fast Fring - microstructural benefits, Trans. J. Br. Ceram. Soc. 80 (1981) 147–148.

[19] A.K. Hofer, A. Kocjan, R. Bermejo, High-strength lithography-based additive manufacturing of ceramic components with rapid sintering, Addit. Manuf. 59 (2022) 103141, https://doi.org/10.1016/j.addma.2022.103141.

[20] A.K. Hofer, A. Kocjan, R. Bermejo, Templated grain growth in rapid sintered 3D-printed alumina ceramics, Open Ceram. 15 (2023) 100428, https://doi.org/10.1016/j.oceram.2023.100428.

[21] C. Wang, W. Ping, Q. Bai, H. Cui, R. Hensleigh, R. Wang, A.H. Brozena, Z. Xu, J. Dai, Y. Pei, C. Zheng, G. Pastel, J. Gao, X. Wang, H. Wang, J. Zhao, B. Yang, J. Luo, Y. Mo, B. Dunn, L. Hu, A general method to synthesize and sinter bulk ceramics in seconds, Science 368 (2020) (1979) 521–526.

[22] M. Biesuz, T.H. de Beauvoir, E. De Bona, M. Cassetta, C. Manière, V.M. Sglavo, C. Estournès, Ultrafast high-temperature sintering (UHS) vs. conventional sintering of 3YSZ: microstructure and properties, J. Eur. Ceram. Soc. 44 (2024) 4741–4750, https://doi.org/10.1016/j.jeurceramsoc.2024.01.064.

[23] S. Bhandari, C. Manière, F. Sedona, E. De Bona, V.M. Sglavo, P. Colombo, L. Fambri, M. Biesuz, G. Franchin, Ultra-rapid debinding and sintering of additively manufactured ceramics by ultrafast high-temperature sintering, J. Eur. Ceram. Soc. 44 (2024) 328–340, https://doi.org/10.1016/j.jeurceramsoc.2023.08.040.

[24] S. Bhandari, O. Hanzel, M. Kermani, V.M. Sglavo, M. Biesuz, G. Franchin, Rapid debinding and sintering of alumina ceramics fabricated by direct ink writing, J. Eur. Ceram. Soc. 45 (2025) 117144, https://doi.org/10.1016/j.jeurceramsoc.2024.117144.

[25] D. Kuscer, A. Kocjan, M. Majcen, A. Meden, K. Radan, J. Kovač, B. Malič, Evolution of phase composition and microstructure of sodium potassium niobate –based ceramic during pressure-less spark plasma sintering and post-annealing, Ceram. Int. 45 (2019) 10429–10437, https://doi.org/10.1016/j.ceramint.2019.02.102.

[26] S. Bhandari, P. Veteška, G. Vajpayee, M. Hinterstein, Ľ. Bača, Z. Hajdúchová, Z. Špitalský, G. Franchin, M. Janek, Material-extrusion based additive manufacturing of BaTiO3 ceramics: from filament production to sintered properties, Addit. Manuf. 88 (2024) 104238, https://doi.org/10.1016/j.addma.2024.104238.

[27] https://zetamix.fr/en/produit/zetamix-alumina-filament/, (n.d.).

[28] L. Gorjan, A. Dakskobler, T. Kosmač, Strength evolution of injection-molded ceramic parts during wick-debinding, J. Am. Ceram. Soc. 95 (2012) 188–193, https://doi.org/10.1111/j.1551-2916.2011.04872.x.

[29] G. Anstis, P. Chantikul, B. Lawn, D. Marshall, A critical evaluation of indentation techniques for measuring fracture toughness: I, direct crack measurements, J. Am. Ceram. Soc. 64 (1981) 533–538.

[30] K. Tanaka, Elastic/plastic indentation hardness and indentation fracture toughness: the inclusion core model, 1987.

[31] A.E. Costa, A. Ferreira da Silva, O.Sousa Carneiro, A study on extruded filament bonding in fused filament fabrication, Rapid Prototyp. J. 25 (2019) 555–565, https://doi.org/10.1108/RPJ-03-2018-0062.

[32] M. Spoerk, F. Arbeiter, H. Cajner, J. Sapkota, C. Holzer, Parametric optimization of intra- and inter-layer strengths in parts produced by extrusion-based additive manufacturing of poly(lactic acid), J. Appl. Polym. Sci. 134 (2017), https://doi.org/10.1002/app.45401.

[33] H. Li, Y. Liu, Y. Liu, Q. Zeng, K. Hu, Z. Lu, J. Liang, Effect of debinding temperature under an argon atmosphere on the microstructure and properties of 3D-printed alumina ceramics, Mater. Charact. 168 (2020) 110548, https://doi.org/10.1016/j.matchar.2020.110548.

[34] N.A. Conzelmann, L. Gorjan, F. Sarraf, L.D. Poulikakos, M.N. Partl, C.R. Müller, F. J. Clemens, Manufacturing complex Al2O3 ceramic structures using consumer-grade fused deposition modelling printers, Rapid Prototyp. J. 26 (2020) 1035–1048, https://doi.org/10.1108/RPJ-05-2019-0133.

[35] C. Tosto, M. Bragaglia, F. Nanni, G. Recca, G. Cicala, Fused filament fabrication of alumina/polymer Filaments for obtaining ceramic parts after debinding and sintering processes, Mater 15 (2022) 7399, https://doi.org/10.3390/ma15207399.

[36] L. Gorjan, C. Galusca, M. Sami, T. Sebastian, F. Clemens, Effect of stearic acid on rheological properties and printability of ethylene vinyl acetate based feedstocks for fused filament fabrication of alumina, Addit. Manuf. 36 (2020) 101391, https://doi.org/10.1016/j.addma.2020.101391.

[37] M. Staudacher, T. Lube, E. Schwarzer-Fischer, J. Abel, M. Reichel, N. Lorenz, L. Gottlieb, S. Long, F. Fehleisen, U. Scheithauer, Strength limiting defects in additively manufactured ceramics, Open Ceram. 24 (2025) 100858, https://doi.org/10.1016/j.oceram.2025.100858.

[38] Y. Tao, F. Kong, Z. Li, J. Zhang, X. Zhao, Q. Yin, D. Xing, P. Li, A review on voids of 3D printed parts by fused filament fabrication, J. Mater. Res. Technol. 15 (2021) 4860–4879, https://doi.org/10.1016/j.jmrt.2021.10.108.

[39] D.E. Garcia, J. Seidel, R. Janssen, N. Claussen, Fast Firing of Alumina, J. Eur. Ceram. Soc. 15 (1995) 935–938.

[40] D. Chen, M. Mayo, Rapid rate sintering of nanocrystalline ZrO2− 3 mol% Y2O3, J. Am. Ceram. Soc. 79 (1996) 906–912. http://onlinelibrary.wiley.com/doi/10.1111/j.1151-2916.1996.tb08524.x/abstract. accessed February 24, 2014.

[41] V. Prajzler, S. Průša, K. Maca, Rapid pressure-less sintering of fine grained zirconia ceramics: explanation and elimination of a core-shell structure, J. Eur. Ceram. Soc. 39 (2019) 5309–5319, https://doi.org/10.1016/j.jeurceramsoc.2019.07.053.

[42] M. Mayo, Processing of nanocrystalline ceramics from ultrafine particles, Int. Mater. Rev. 41 (1996) 85–115, in: http://scholar.google.com/scholar?hl=en&btnG=Search&q=intitle:Processing+of+nanocrystalline+ceramics+from+ultrafine+particles#0. accessed January 30, 2014.

[43] A.W. Searcy, Theory for sintering in temperature gradients: role of long-range, mass transport, J. Am. Ceram. Soc. 70 (1987), https://doi.org/10.1111/j.1151-2916.1987.tb04967.x. C–61-C-62.

[44] W. Ji, J. Zhang, W. Wang, Z. Fu, R. Todd, The microstructural origin of rapid densification in 3YSZ during ultra-fast firing with or without an electric field, J. Eur. Ceram. Soc. 40 (2020) 5829–5836, https://doi.org/10.1016/j.jeurceramsoc.2020.07.027.

[45] V. Nečina, W. Pabst, Influence of the heating rate on grain size of alumina ceramics prepared via spark plasma sintering (SPS), J. Eur. Ceram. Soc. 40 (2020) 3656–3662, https://doi.org/10.1016/j.jeurceramsoc.2020.03.057.

[46] T.L. Bergman, A.S. Lavine, F.P. Incropera, D.P. DeWitt, Fundamentals of Heat and Mass Transfer, 8th ediiton, Wiley, 2018.

[47] E. Novitskaya, K. Karandikar, K. Cummings, M. Mecartney, O.A. Graeve, Hall-Petch effect in binary and ternary alumina /zirconia / spinel composites, J. Mater. Res. Technol. 11 (2021) 823–832, https://doi.org/10.1016/j.jmrt.2021.01.058.

[48] D.E. García, A.N. Klein, D. Hotza, Advanced ceramics with dense and fine-grained microstructures through fast firing, Rev. Adv. Mater. Sci. 30 (2012) 273–281.

[49] Z. Shen, L. Liu, X. Xu, J. Zhao, M. Eriksson, Y. Zhong, E. Adolfsson, Y. Liu, A. Kocjan, Fractography of self-glazed zirconia with improved reliability, J. Eur. Ceram. Soc. 37 (2017) 4339–4345, https://doi.org/10.1016/j.jeurceramsoc.2017.03.008.

[50] D. Li, Y. Liu, Y. Zhong, L. Liu, E. Adolfsson, Z. Shen, Dense and strong ZrO 2 ceramics fully densified in <15 min, Adv. Appl. Ceram. 118 (2019) 23–29, https://doi.org/10.1080/17436753.2018.1449580.

[51] D. Jiang, D.M. Hulbert, U. Anselmi-Tamburini, T. Ng, D. Land, A.K. Mukherjee, Optically transparent polycrystalline Al2O3 produced by spark plasma sintering, J. Am. Ceram. Soc. 91 (2008) 151–154, https://doi.org/10.1111/j.1551-2916.2007.02086.x.

[52] G. Bernard-Granger, N. Benameur, C. Guizard, M. Nygren, Influence of graphite contamination on the optical properties of transparent spinel obtained by spark plasma sintering, Scr. Mater. 60 (2009) 164–167, https://doi.org/10.1016/j.scriptamat.2008.09.027.

[53] A. Kocjan, M. Češnovar, D. Vengust, T. Kosmač, A. Dakskobler, Translucent yttria- and silica-doped mullite ceramics with anisotropic grains produced by spark plasma sintering, J. Am. Ceram. Soc. 99 (2016) 3090–3096, https://doi.org/10.1111/jace.14302.

[54] K. Morita, B.-N. Kim, H. Yoshida, K. Hiraga, Y. Sakka, Spectroscopic study of the discoloration of transparent MgAl2O4 spinel fabricated by spark-plasma-sintering (SPS) processing, Acta. Mater. 84 (2015) 9–19, https://doi.org/10.1016/j.actamat.2014.10.030.

[55] K. Morita, B.N. Kim, H. Yoshida, K. Hiraga, Y. Sakka, Distribution of carbon contamination in oxide ceramics occurring during spark-plasma-sintering (SPS) processing: II - effect of SPS and loading temperatures, J. Eur. Ceram. Soc. 38 (2018) 2596–2604, https://doi.org/10.1016/j.jeurceramsoc.2017.12.004.

[56] G.C. Wei, Transparent ceramics for lighting, J. Eur. Ceram. Soc. 29 (2009) 237–244, https://doi.org/10.1016/j.jeurceramsoc.2008.03.018.

[57] Y. Feng, H. Hou, B. Yang, B. Yang, F. Zi, Decomposition of solid alumina in the presence of carbon in vacuum, Vacuum 145 (2017) 169–173, https://doi.org/10.1016/j.vacuum.2017.08.043.

[58] S. Bhandari, T. Heim, E. De Bona, V.M. Sglavo, W. Rheinheimer, M. Biesuz, G. Franchin, Rapid processing of Al2O3 ceramics by fused filament fabrication and ultrafast high-temperature debinding and sintering, J. Alloys Compd. 1017 (2025) 178812, https://doi.org/10.1016/j.jallcom.2025.178812.

[59] G. Molénat, L. Durand, J. Galy, A. Couret, Temperature control in spark plasma sintering: an FEM approach, J. Metall. 2010 (2010) 1–9, https://doi.org/10.1155/2010/145431.

[60] "SIGRATHERM® Download-Center | SGL Carbon." https://www.sglcarbon.com/en/markets-solutions/material-downloads/downloads-sigratherm/(accessed Feb. 26, 2024), (n.d.).

[61] A. Pavia, L. Durand, F. Ajustron, V. Bley, G. Chevallier, A. Peigney, C. Estournès, Electro-thermal measurements and finite element method simulations of a spark plasma sintering device, J. Mater. Process. Technol. 213 (2013) 1327–1336, https://doi.org/10.1016/j.jmatprotec.2013.02.003.

[62] M. Schüßler, M. Auweter-Kurtz, G. Herdrich, S. Lein, Surface characterization of metallic and ceramic TPS-materials for reusable space vehicles, Acta Astronaut. 65 (2009) 676–686, https://doi.org/10.1016/j.actaastro.2009.01.048.